metals

MDPI

Article

Effect of Hydrogen Content on the Microstructure, Mechanical Properties, and Fracture Mechanism of Low-Carbon Lath Martensite Steel

Boris Yanachkov [1,*], Yana Mourdjeva [1], Kateryna Valuiska [1,2], Vanya Dyakova [1], Krasimir Kolev [1], Julieta Kaleicheva [1], Rumyana Lazarova [1] and Ivaylo Katzarov [1,3]

[1] Institute of Metal Science, Equipment, and Technologies with Center of Hydro- and Aerodynamics "Acad. A. Balevski" at the Bulgarian Academy of Sciences, 67 "Shipchenski prohod", 1574 Sofia, Bulgaria; kateryna@ims.bas.bg (K.V.); kkolev@ims.bas.bg (K.K.); r.lazarova@ims.bas.bg (R.L.)
[2] Frantsevich Institute for Problems of Materials Science at National Academy of Sciences Ukraine, 3 Omelyan Pritsak (Krzhizhanovskyi), 03142 Kyiv, Ukraine
[3] National Center for Mechatronics and Clean Technologies, 8 Kliment Ohridski Blvd., Building 8, 1756 Sofia, Bulgaria
* Correspondence: byanachkov@ims.bas.bg

Abstract: The effect of hydrogen content on the microstructure, mechanical properties, and fracture mechanisms of low-carbon lath martensitic steel was investigated using both experimental methods and atomistic modeling. Tensile testing revealed a transition in the fracture behavior with increases in hydrogen concentration. Specifically, at a hydrogen content of 0.44 wppm, a shift from transgranular to intergranular fractures was observed. The most probable cause of hydrogen embrittlement was identified to be HELP-mediated HEDE. As the hydrogen concentration increased, the dislocation density in close-packed planes, such as (111) and (100), was found to rise. The key differences between the hydrogen-free and hydrogen-charged specimens were the localization and density of dislocations, as well as the change in the distribution of slip bands. Atomistic modeling supported these experimental findings, showing that "quasi-cleavage" cracks predominantly initiate at block boundaries with higher local hydrogen accumulation. These results underscore the significant role of hydrogen in modifying both the microstructural characteristics and fracture behavior of low-carbon martensitic steel, with important implications for its performance in hydrogen-rich environments.

Keywords: hydrogen embrittlement; lath martensite; HEDE; HELP; tensile test; fracture

check for updates

Citation: Yanachkov, B.; Mourdjeva, Y.; Valuiska, K.; Dyakova, V.; Kolev, K.; Kaleicheva, J.; Lazarova, R.; Katzarov, I. Effect of Hydrogen Content on the Microstructure, Mechanical Properties, and Fracture Mechanism of Low-Carbon Lath Martensite Steel. *Metals* **2024**, *14*, 1340. https://doi.org/10.3390/met14121340

Academic Editors: Kai Xu and Guiying Qiao

Received: 21 October 2024
Revised: 13 November 2024
Accepted: 20 November 2024
Published: 26 November 2024

Copyright: © 2024 by the authors. Licensee MDPI, Basel, Switzerland. This article is an open access article distributed under the terms and conditions of the Creative Commons Attribution (CC BY) license (https://creativecommons.org/licenses/by/4.0/).

1. Introduction

In recent years, hydrogen has emerged as an environmentally friendly fuel, highlighting the need to address the challenges of its safe and efficient storage and transportation. Researchers are exploring the potential in utilizing existing low-carbon steel pipeline infrastructure for both natural gas and hydrogen transport [1,2]. As a result, there is growing interest in understanding the impact of hydrogen on the properties of low-carbon steel, the most widely used material for pipeline construction.

Hydrogen embrittlement (HE) refers to the degradation of the mechanical properties of metals and alloys caused by the presence of dissolved atomic hydrogen (H) [3]. Even low concentrations of hydrogen can induce crack formation. Although the detrimental effects of hydrogen on the mechanical properties of metals and alloys have been extensively studied [4,5], the detailed mechanisms underlying HE remain poorly understood. Two primary mechanisms proposed to explain HE are "hydrogen-enhanced decohesion" (HEDE) and "hydrogen-enhanced localized plasticity" (HELP). The HELP mechanism [6–8] suggests that HE arises from increased dislocation mobility in the presence of hydrogen, which leads to a reduction in material strength. Additionally, hydrogen weakens the elastic interaction

between dislocations and obstacles, diminishing the shielding effect and resulting in dislocation pile up, which contributes to material degradation [9]. In contrast, HEDE links hydrogen embrittlement to the weakening of atomic bonds at grain boundaries and phase interfaces due to hydrogen segregation [10,11]. This reduction in cohesive strength at the boundaries leads to crack initiation and propagation along these regions when the applied stress exceeds the material's cohesive strength.

Lath martensite steels are commonly used for their favorable plasticity and toughness. However, martensite is known to be particularly susceptible to hydrogen embrittlement (HE) due to the high density of lath/block boundaries and dislocations, which are prone to HE initiation [12,13]. A lath martensite grain is composed of packets that include blocks and sub-blocks formed by parallel martensitic laths with a (110) habit plane. The lath boundaries within the blocks have a low twist angle ($\varphi < 15^{o}$), while block boundaries can be either low- or high-angle twist boundaries [14,15]. Experimental observations of fractured surfaces reveal that the presence of hydrogen alters the fracture mode. In the absence of hydrogen, transgranular cracks form due to the plastic coalescence of microvoids. However, with hydrogen present, these transgranular cracks transform into "quasi-cleavage" cracks along the lath/block boundaries, or into intergranular "flat" cracks along prior austenite grain boundaries (GBs). Some researchers have proposed that "quasi-cleavage" occurs when slip systems intersect block boundaries, where hydrogen reduces the cohesive strength, facilitating crack initiation and propagation [12].

Hydrogen is believed to be trapped at the prior austenite or lath/block boundaries [16–18]. Localization of hydrogen at these interfaces has been linked to hydrogen-enhanced decohesion (HEDE), which contributes to hydrogen embrittlement (HE) in lath martensite steels [19]. Additionally, the presence of ferrite in these steels may facilitate other HE mechanisms, such as hydrogen-enhanced localized plasticity (HELP), which involve increased dislocation activity in ferrite. The literature suggests that multiple HE mechanisms may concurrently operate in lath martensite steels [20].

It is well established [1,2] that hydrogen concentration significantly influences the mechanical properties of metals, particularly at temperatures near room temperature. In [1], a model was proposed that accounts for the effects of hydrogen on the plasticity and embrittlement of metals, as well as for their deformation and failure mechanisms. A model describing the dependence of the strength of low-carbon pipe steels on hydrogen concentration was presented in [21,22]. This study found that, within a specific range of hydrogen concentrations ($1.77–2.09 \times 10^{-6}$ mol/cm^3), the failure mode of the steel shifted sharply from ductile to brittle. However, due to the lack of a comprehensive theory explaining the mechanisms of hydrogen embrittlement (HE), further analysis was needed to clarify its origin in lath martensite steels. This would provide valuable insights for improving the microstructural design of high-strength martensitic steels.

In the present study, we investigated the influence of varying hydrogen concentrations on the microstructure, mechanical properties, and failure mechanisms of low-carbon lath martensitic steel specimens. The primary goal of this work was to enhance our understanding of the HE mechanisms in lath martensitic structures by employing a combination of experimental techniques and numerical modeling.

2. Materials and Methods

2.1. Materials

The base material investigated in this study was steel S355J2C (1.0579) (EN 10162: 2003) [23]. The chemical composition of the steel was analyzed using an optical emission spectrometer (Q4 TASMAN Q101750–C 130, BRUKER AXS, Berlin, Germany). The results are presented in Table 1.

Table 1. Chemical composition of the investigated steel.

Element	C	Si	Mn	P	S	Fe
Wt. %	0.19	0.29	1.10	0.0010	0.0032	Bal.

A plate measuring 60 mm × 120 mm × 6 mm was cut from a cold-rolled steel beam, with the 120 mm length oriented parallel to the rolling direction (RD) of the beam.

To achieve a lath martensitic microstructure, the steel plate was heated at 1150 °C for 30 min in a Carbolite tube furnace (Aston Lane Hope, Sheffield S30 2RR, UK) under an argon atmosphere. The plate was then quenched in ice water containing 15% NaCl. Since martensite is known to be the most hydrogen-sensitive microstructure when compared to others such as ferrite, pearlite, and bainite [24–26], the plate was immediately immersed in liquid nitrogen for 60 min to promote the transformation of any residual austenite into martensite.

To achieve the primary research objective of this study, it was necessary to prepare and test steel samples with varying hydrogen concentrations. To obtain these samples, we drew on the methodology of previous research [27,28], which demonstrated a relationship between the "oxidation current" and the concentration of the hydrogen recombination inhibitor NH_4SCN when it is applied to the charge side of the permeability cell. Specifically, Ref. [28] showed that, for a fixed current density on the charge side, the oxidation current on the output side varied with the concentration of NH_4SCN, corresponding to a higher hydrogen flux through the sample. That study also found that the presence of NH_4SCN in the electrolyte altered the slope of the Tafel plot, indicating inhibition of the hydrogen recombination reaction and resulting in an increased hydrogen uptake.

The electrolyte compositions used to achieve different hydrogen concentrations in the investigated steel are outlined below.

An alkaline electrolyte, consisting of 0.1 M of NaOH and a hydrogen recombination inhibitor (NH_4SCN), was used for hydrogen saturation as it does not induce hydrogen damage during testing. Hydrogen concentrations were varied by adjusting the concentration of NH_4SCN while maintaining a fixed current density of 3 mA/cm^2. The specific electrolyte compositions were as follows: (i) 0.1 M of NaOH; (ii) 0.1 M of NaOH + 1 g/L of NH_4SCN; and (iii) 0.1 M of NaOH + 6 g/L of NH_4SCN.

In this article, the steel specimens are designated as follows: specimens not charged with hydrogen are labeled **A**; specimens with the lowest hydrogen content, which are charged from the 0.1 M of NaOH electrolyte, are labeled **B**; specimens charged using the 0.1 M of NaOH + 1 g/L of NH_4SCN electrolyte are labeled **C**; and specimens charged using the 0.1 M of NaOH + 6 g/L of NH_4SCN electrolyte are labeled **D**. Two specimens were prepared for each type (**A**, **B**, **C**, and **D**). The hydrogen concentration in each specimen corresponds to its designation, in the following order: **A** < **B** < **C** < **D**, with **A** having 0 wppm, **B** containing hydrogen in the range of 0 < **B** < 0.44 wppm, **C** having 0.44 wppm, and **D** exceeding 0.44 wppm. The hydrogen concentration of Specimen **C** was determined to be 0.44 wppm. Measurement was conducted using the G8 GALILEO analyzer by BRUKER. The sample was charged in an electrolyte under predefined conditions and then immediately analyzed using the Thermal Desorption Mass Spectrometry (TDMS) technique, with an infrared heating furnace operating at a heating rate of 1200 K/min. The hydrogen concentrations for Specimens **B** and **D** were not directly measured.

2.2. Characterization Methods

The steel microstructure after heat treatment was characterized using light microscopy (LM), X-ray diffraction (XRD), scanning electron microscopy (SEM), and transmission electron microscopy (TEM).

For LM observations, a section of the heat-treated plate was prepared by mechanical grinding using abrasive papers with grits #320, 400, 600, 1200, and 2000, followed by a two-step polishing process with OPS (oxide polishing suspension). The specimen was then

etched using a 4% solution of HNO_3 in ethyl alcohol. Microhardness measurements were conducted using a MicroDuromat 4000 microhardness tester, with a load of 0.05 kgf, an application time of 10 s, and a holding time of 10 s. The reported microhardness value was the average of five measurements.

X-ray diffraction (XRD) analysis was performed to determine the phase composition of the steel after heat treatment. Diffraction patterns were recorded using an X-ray diffractometer TDM-10 (by Dandong Tongda Science and Technology Co., Ltd., Dandong, China) equipped with a scintillation detector, utilizing Ni-filtered Cu Kα radiation. The X-ray tube was operated at 35 kV and 30 mA. Data were collected in the 2θ range from 35° to 120°, with a step size of 0.01° and a scan speed of 0.3°/min. Phase analysis was carried out using the PDF-2 ICDD database and analyzed with MDI/Jade 6.5 software.

X-ray diffraction line broadening studies were carried out using a Philips PW 1050 diffractometer (by Philips Analytical, Almelo, The Netherlands) equipped with a Cu tube and a scintillation detector. The lattice parameters, microstrains, and crystallite sizes of the steel samples were determined using HighScore Plus 4.5/Malvern Panalytical analysis software. Dislocation densities ρ were calculated using the Williamson–Hall method [29–32]:

$$\rho = \sqrt{\rho_S \rho_D}, \tag{1}$$

where ρ_S is the dislocation density calculated from the broadening of the diffraction lines related to the microstrains, and ρ_D is the dislocation density calculated from the broadening of the diffraction lines related to the crystallite size.

$$\rho_S = \frac{k\varepsilon^2}{Fb^2}, \tag{2}$$

$$\rho_D = \frac{3n}{D^2}, \tag{3}$$

where ε is the microstrain, b is the Burger's vector ($b = a\sqrt{2}$ for all the samples in this study), F is an interaction factor assumed to be 1, k is a material constant assumed as 14.4 for body-centered cubic (bcc) metals, D is the crystallite size, and n is assumed as 1.

Fractographic examinations of the fractured specimens from the tensile tests were conducted on surfaces perpendicular to the tensile direction. The surfaces examined had a length of 6 mm and a width of 0.5–0.8 mm. Observations were made using a HIROX 5500 scanning electron microscope (SEM, HIROX Europe, Limonest, France) equipped with a BRUKER EXDS system (BRUKER Co., Berlin, Germany).

Transmission electron microscopy (TEM) analysis was performed on the microstructure of specimens before and after the relaxation tests. The specimen designations (A, B, C, and D) correspond to their hydrogen contents. TEM observations were carried out with a high-resolution transmission electron microscope (HRTEM, JEM 2100, JEOL Ltd., Akishima, Japan) at an accelerating voltage of 200 kV using selected area electron diffraction (SAED) at magnifications ranging from 6 K to 20 K. The specimens were electropolished on a TENUPOL 5 with an "A2" electrolyte under standard conditions. The observation plane was perpendicular to the direction of the applied load during the test.

2.3. Tensile and Relaxation Tests

Eight tensile test specimens were cut from the steel plate using a wire erosion machine, following the guidelines of the BDS EN ISO 6892-1:2020 standard [33], after heat treatment. The geometry and dimensions of the specimens are shown in Figure 1.

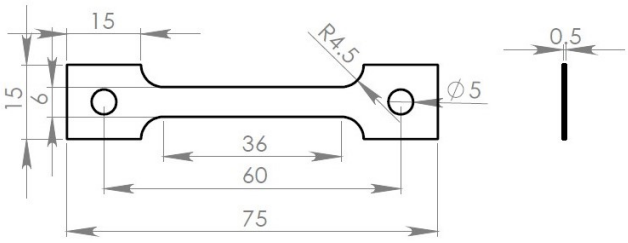


Figure 1. Schematic diagram of the specimens used for tensile tests.

The dimensions of the specimens were selected to fit the in situ hydrogen charging cell. The tensile direction of the specimens aligned with the rolling direction (RD) of the steel beam. After cutting, the specimens were ground on both sides using #600 abrasive paper.

To investigate the effect of the different hydrogen contents on the failure mechanism of low-carbon lath martensitic steel, four types of specimens were subjected to tensile testing. All tests were performed on a ZWICK ROELL HA 250 servo-hydraulic mechanical testing system (Germany). The test strain rate was set to 10^{-4} s^{-1} based on literature recommendations [34].

Specimen A was tensile-tested in air. To obtain stress–strain curves for specimens with varying hydrogen contents, tensile tests were performed on Specimens B, C, and D, which were hydrogen-charged in situ for 60 min at a current density of 3 mA/cm^2 using three different electrolytes. The electrochemical charging was conducted in a specially designed in situ electrochemical tensile cell [35]. The galvanostatic charging technique described in [27,28] was employed. The 60-minute charging time for the 0.5 mm-thick specimens was selected based on data of the hydrogen penetration and diffusion in steels [25,36].

Relaxation tests were carried out on a ZWICK ROELL HA 250 testing machine using the in situ electrochemical charging cell. The specimens were placed in the cell with electrolytes and charged for 60 min at a current density of 3 mA/cm^2. After the charging period, the specimens were loaded beyond the yield point, and the strain was held constant for 20 s while the stress relaxation was recorded. This process was repeated for a total of 10 cycles.

3. Results and Discussion

3.1. Light Microscopy

The microstructure of the quenched plate at two magnifications is shown in Figure 2.

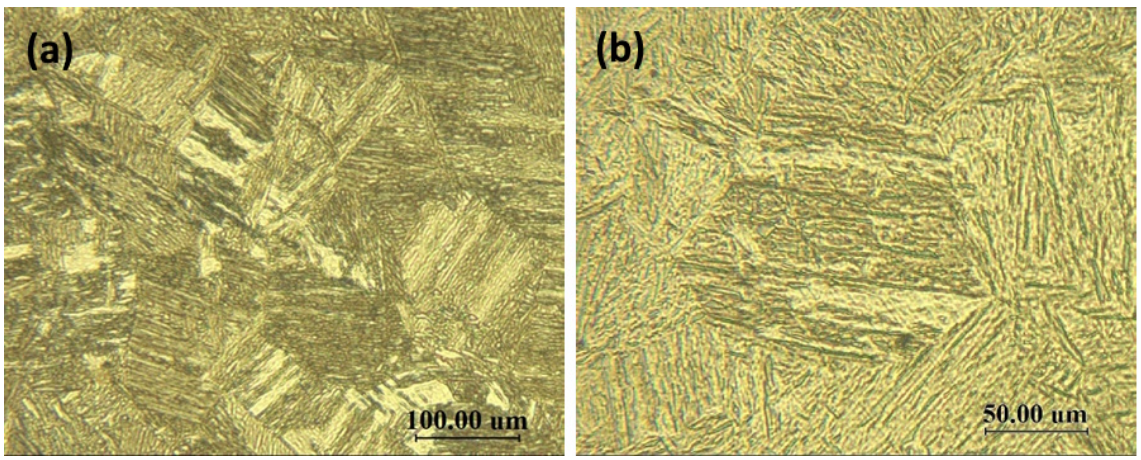


Figure 2. Microstructure of the investigated steel after quenching: (**a**) general view, and (**b**) a magnified view where the prior austenite grains (PAGs) can be recognized.

The microstructure exhibited a typical lath martensite structure, with laths arranged in blocks that formed packets within the prior austenite grains (PAGs) (Figure 2a). The

average block width in the investigated sample was approximately 30 µm (Figure 2a). The yield strength of the low-carbon steels with a lath martensite structure was closely related to both the packet size and the block size (width). According to [37], the block size is a key structural parameter influencing the strength–structure relationship.

The mean diameter of the prior austenite grains (PAGs) was found to be approximately 110 µm (Figure 2b). The typical width of the martensite laths was less than 1 µm [15]. Using the secant line method, the lath width was measured in three fields of view at 1000× magnification, yielding an average value of approximately 0.9 µm for the investigated samples. Lath martensite forms at relatively high temperatures (the M_s temperature of the investigated steel being 370 °C ([38,39])). At these temperatures, dislocation glide is the dominant mechanism for accommodating deformation. The investigated samples also contained a small amount of self-tempered martensite, as shown in Figure 2a. Using a quantitative metallographic method, the volume fraction of the self-tempered martensite was determined to be approximately 2.9% for each sample. However, studying the influence of this self-tempered martensite on the steel's properties was beyond the scope of this work. No other phases were optically observed.

The measured microhardness of the lath martensite microstructure in the as-quenched state was 480 kgf/mm^2.

3.2. X-Ray Diffraction

The result of the X-ray analysis is displayed in Figure 3.

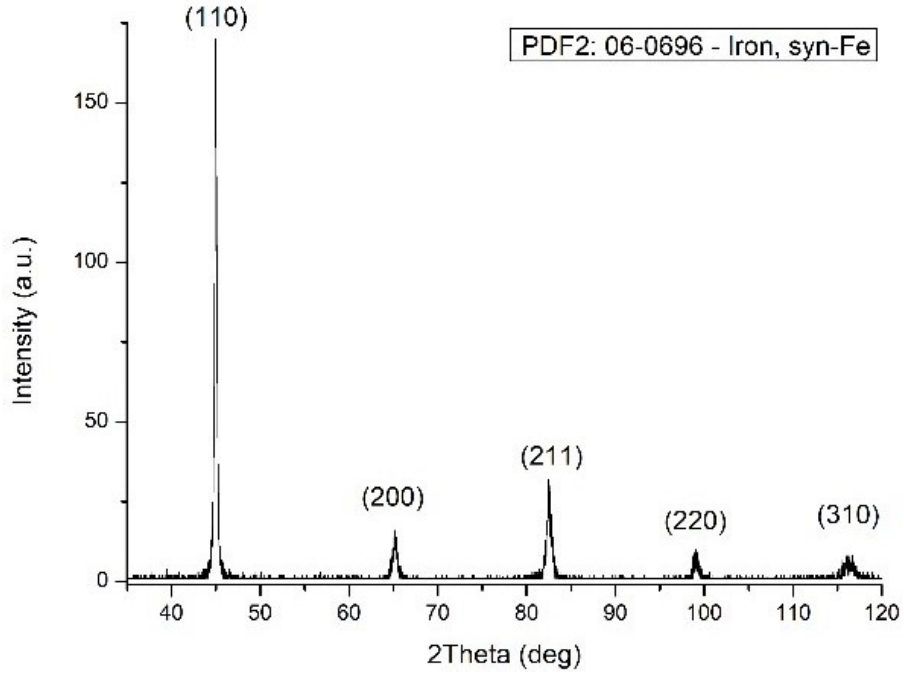


Figure 3. X-ray diffraction pattern of the investigated steel after heat treatment.

The peaks corresponded to a body-centered cubic (BCC) lattice with an Im-3m space group. The BCC phase is typical in low-carbon steels with a martensite structure [40]. This occurs because the carbon content is insufficient to induce lattice distortion, which would otherwise lead to the formation of a body-centered tetragonal (BCT) phase, which is characteristic of high-carbon martensitic steels.

The analysis revealed that the steel specimen contained no detectable retained austenite (FCC phase), or the quantity of the retained austenite was below the detection limit of this method (3%). After refinement, the calculated cell parameter was: a = 2.86219 Å, with a cell volume of V = 23.45 Å^3.

The diffraction lines exhibited broadening due to the structural fragmentation from quenching and the presence of microstrains associated with dislocations in the martensitic structure. Dislocation density can be estimated by analyzing the diffraction line profiles, which are affected by both microstrains and crystallite size [29–32,41,42]. A slight increase in dislocation density was observed in the sample subjected to hydrogen charging (Specimen D), with a value of 1.83×10^{11} cm^{-2} compared to 1.57×10^{11} cm^{-2} for the post-quenching specimen (A), which was not hydrogen-charged.

3.3. Tensile Tests

The results of the tensile tests for the base steel Specimen A (tested in air) and the in situ tests for the specimens with varying hydrogen concentrations (B, C, and D) are presented in Table 2. The data in Table 2 were derived from the stress–strain curves ($\sigma - \varepsilon$) of each tested specimen. The corresponding engineering stress–strain curves are shown in Figure 4.

Table 2. Data from the stress–strain test of the A, B, C, and D specimens.

Designation of Samples	Max Strength, σ_{max} [MPa]	Max Deformation, ε [%]
A	1372.8	6.30
B	1128.1	3.29
C	1094.5	2.67
D	988.5	1.86

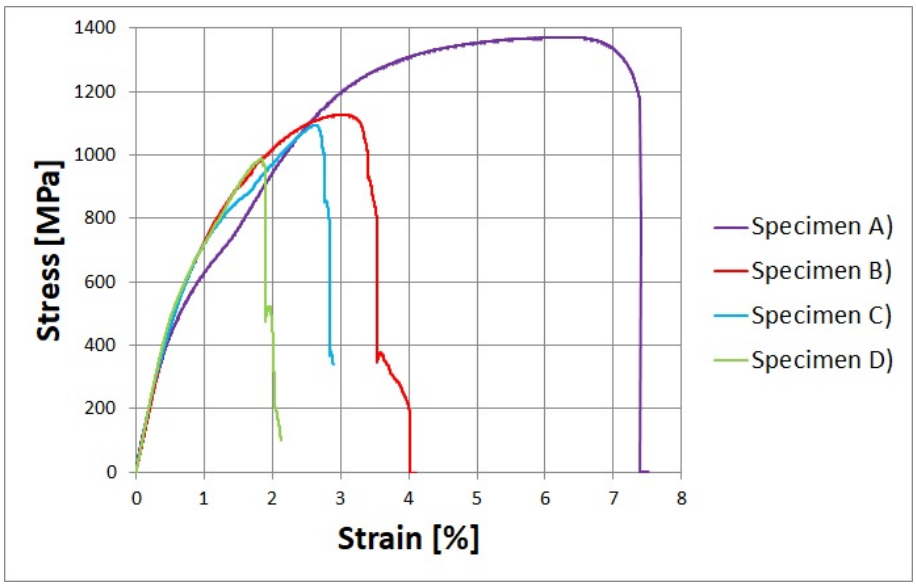


Figure 4. Stress-strain curves of the investigated specimens.

Experimental data showed that, as the hydrogen concentration increased, the ultimate stress of the specimens (σ_{max}) decreased. Small amounts of hydrogen reduced the σ_{max} value of Specimen B by 240 MPa compared to the uncharged Specimen A. As the hydrogen content increased further, the reduction in σ_{max} became more gradual, with a decrease of 34 MPa (Specimen C vs. B) and 106 MPa (Specimen D vs. C), respectively. The decrease in maximum strain ε_{max} from the uncharged Specimen A to the specimen with the highest hydrogen concentration (D) was more than threefold.

3.4. Analysis of the Fractured Surfaces After the Tensile Tests

The fracture surfaces of the tensile-tested Specimens A, B, C, and D are shown in Figures 5–8. In each figure, the (a) panel displays the fully fractured surface of the specimen, while panels (b), (c), (d), etc., highlight the characteristic areas of the fracture surface.

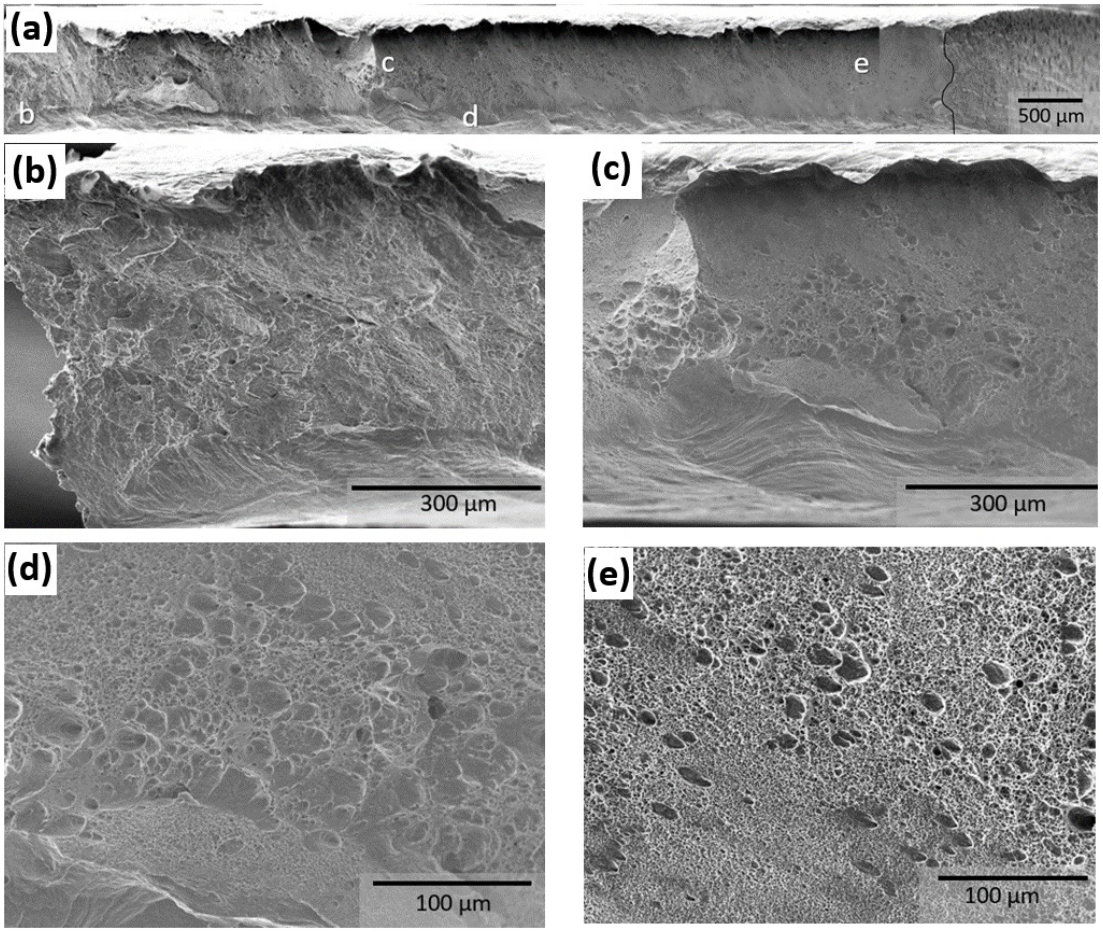


Figure 5. Fracture surface of Specimen A: (**a**)—general view; (**b**–**e**)—magnified views of zones of the general view, where dimples of varying sizes and orientations are observed.

In the hydrogen-free base Specimen A (Figure 5a), fracture entirely occurred through a ductile microvoid coalescence mechanism. At higher magnifications (Figure 5b–e), dimples of varying sizes and orientations were observed along the entire length of the fractured section. Coarser dimples were observed at the left edge of the specimen (Figure 5b), indicating the initiation of failure. The dimple density in this region was relatively low. Some authors [43] refer to this area as the ductile cracking (DC) zone (Figure 5b). The highest density of dimples was found at the right end of the specimen, corresponding to the area where the crack propagation was completed.

Figure 6a shows the fracture surface of Specimen B, which has the lowest hydrogen saturation in the concentration range of 0–0.44 wppm. The fracture mode involves both ductile and brittle mechanisms (Figure 6b). The ductile fracture zones occupy a larger area, while the brittle fracture exhibits a quasi-cleavage pattern. In Figure 6c,e, well-defined facets are visible, with fine "river patterns" that are characteristic of quasi-cleavage. According to [44], such facets are typical of cleavage fracture in hydrogen-charged martensitic steels, and their propagation occurs along the close-packed planes [12,45–49]. The propagation of these facets along the close-packed planes is often interpreted as occurring either along the martensitic lath boundaries [46,50] as these interfaces are generally aligned with the 110 martensitic habit plane, or they are as a result of slip plane decohesion [45]. Figure 6d clearly shows the typical quasi-cleavage features, including "steps" (white arrows) and "ridges" (white ellipses). Some authors define "ridges" as the tops of the "river patterns". According to [43], the topology and orientation of these fine structures within the facets are influenced by the orientation of the martensitic laths or block boundaries. They suggest that the "ridges" form as cracks propagate along these lath or block boundaries. Cracks at these interfaces (white square) are visible in Figure 6c,d,e.

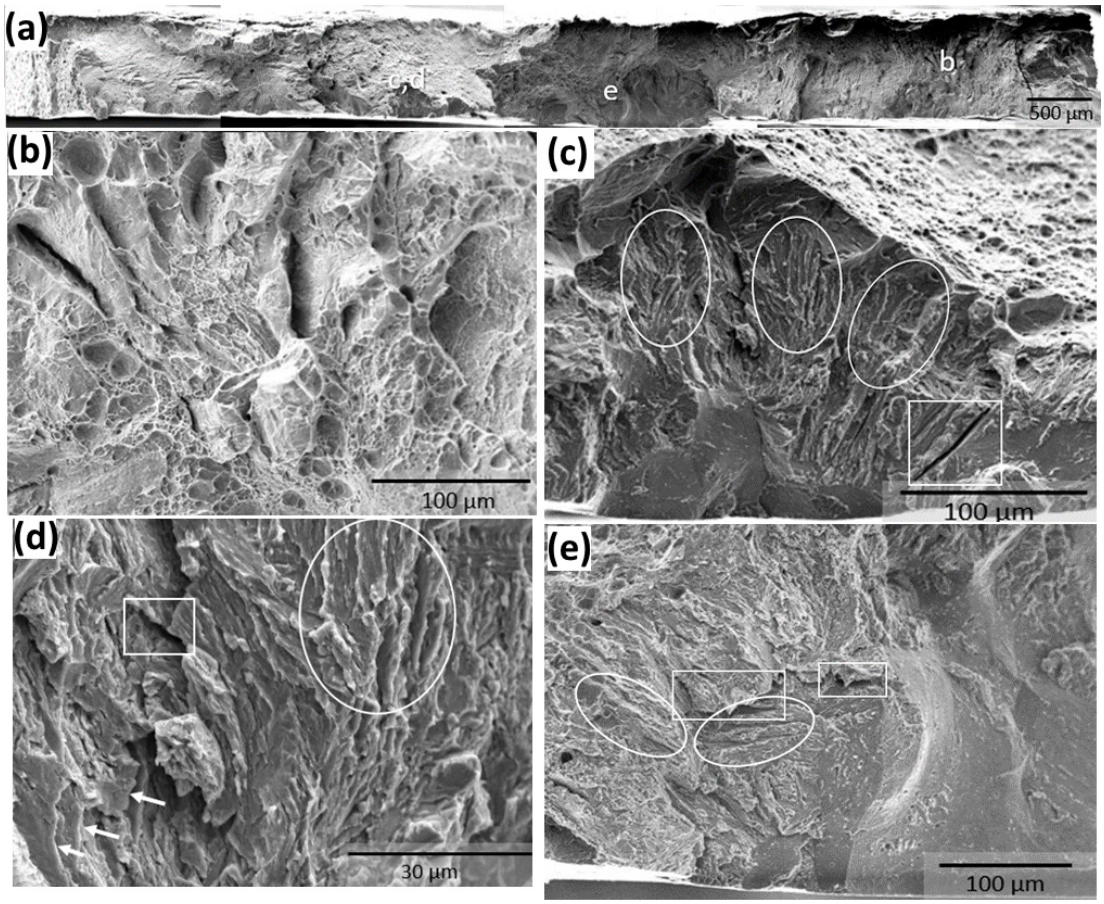


Figure 6. Fracture surface of Specimen B: (**a**)—general view; (**b**)—zone with ductile fracture; (**c**)—zone where can be recognized facet, "river patterns" (white ellipses) and crack (white square); (**d**)—quasi-cleavage features, including "steps" (white arrows) and "ridges" (white ellipse); (**e**)—zone with "ridges" (white ellipses) and cracks (white square).

Figure 7a shows the fractured surface of test Specimen C. As with Specimen B, the fracture occurred via ductile and brittle mechanisms. However, the proportion of areas fractured by ductile mechanisms (as shown in the upper halves of Figure 7c,d) was smaller in Specimen C compared to Specimen B. The dimples in Specimen C were both wider and deeper than those in Specimen B, indicating a more pronounced ductile fracture. The area of brittle fracture zones increased in Specimen C, and these zones were primarily located near the outer surfaces of the specimen. This suggests that the hydrogen concentration was likely higher near the surface than in the central region of the specimen. In addition to quasi-cleavage fracture zones (Figure 7b,d), Specimen C also exhibited well-defined intergranular fracture zones (Figure 7c,e). These cracks propagated along the prior austenite grain boundaries, as shown in Figure 7c,e. The white arrows in Figure 7c highlight the locations of typical brittle fractures.

In Figure 8a, the fractured surface of the specimen with the highest hydrogen concentration (D > 0.44 wppm) is shown. The ratio between the areas fractured by ductile and brittle mechanisms remains consistent. A crack was visible, and it was transversely oriented to the specimen's axis, extending across its entire width (Figure 8c). The ridges, as shown in Figure 8c,d, were oriented in different directions, following the pattern of martensite laths and packets. Intergranular fracture zones were again observed near the outer surfaces of the specimen (Figure 8b,d), where the hydrogen concentration was highest. Notably, cracks along the prior austenite grain boundaries in the intergranular fracture were clearly defined (Figure 8b).

According to the authors of [43], the steps indicated by the white arrows in Figure 8c are formed during the development of a "quasi-cleavage" fracture. These steps correspond to activated slip bands that are inclined along the lath boundaries, intersecting the fracture surface.

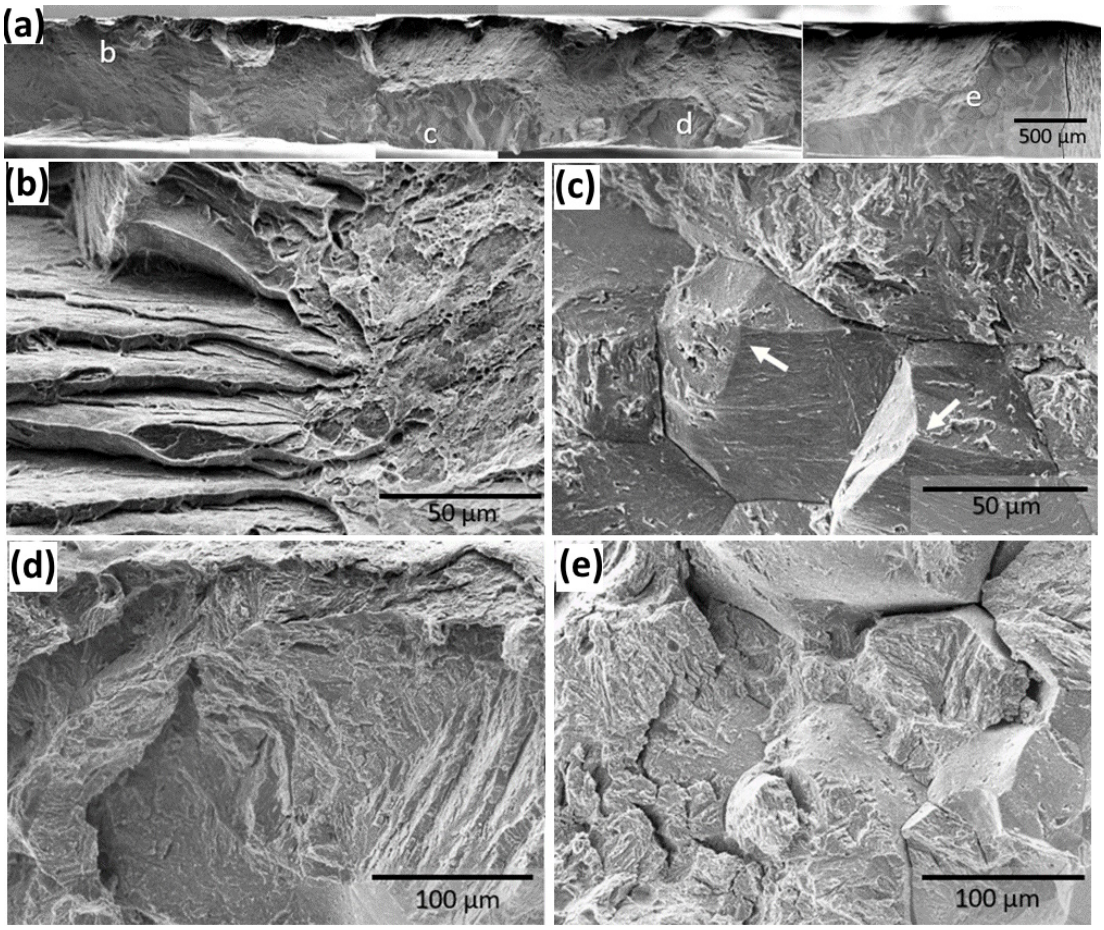


Figure 7. Fracture surface of Specimen C: (**a**)—general view; (**b**,**d**)—quasi-cleavage fracture zones; (**c**,**e**)—intergranular fracture zones with cracks propagated along the prior austenite grain boundaries.

Similar step formations were not observed in the specimens with lower hydrogen concentrations (A and B). The preferred fracture planes will be discussed in greater detail in the TEM observation section.

It was evident that, as the hydrogen concentration increased, the fracture mechanism transitioned from a mix of transgranular and intergranular failure (as observed in Specimen B) to the predominantly intergranular failures shown in Specimens C and D. This transition from transgranular to intergranular fracture has been described by [20] as a shift to a mixed hydrogen embrittlement (HE) mechanism, specifically HELP-mediated HEDE.

In [21], it was established that there exists a characteristic hydrogen concentration, C_H (critical), at which the fracture mechanism of steel changes. When $C_H \leq C_H$ (critical), plastic fracture occurs, while, for $C_H \geq C_H$ (critical), the fracture mechanism becomes brittle. For example, for steel 20, the critical hydrogen concentration, C_H (critical), is relatively low in the range of 1.77–2.09 $\times$ 10^{-6} mol/cm^3. Given that 1 $\times$ 10^{-6} mol/cm^3 is approximately equivalent to 0.15 wppm, the hydrogen concentration in our specimens (ranging from 2 $\times$ 10^{-6} mol/cm^3 to 3 $\times$ 10^{-6} mol/cm^3) falls within the transition zone from ductile to brittle fracture. This corresponds to HELP-mediated HEDE. For the steel specimens in this study, the shift in fracture mechanism occurred at hydrogen concentrations not exceeding

0.44 wppm, which suggests that the critical hydrogen concentration, C_H (critical), was lower than 0.44 wppm.

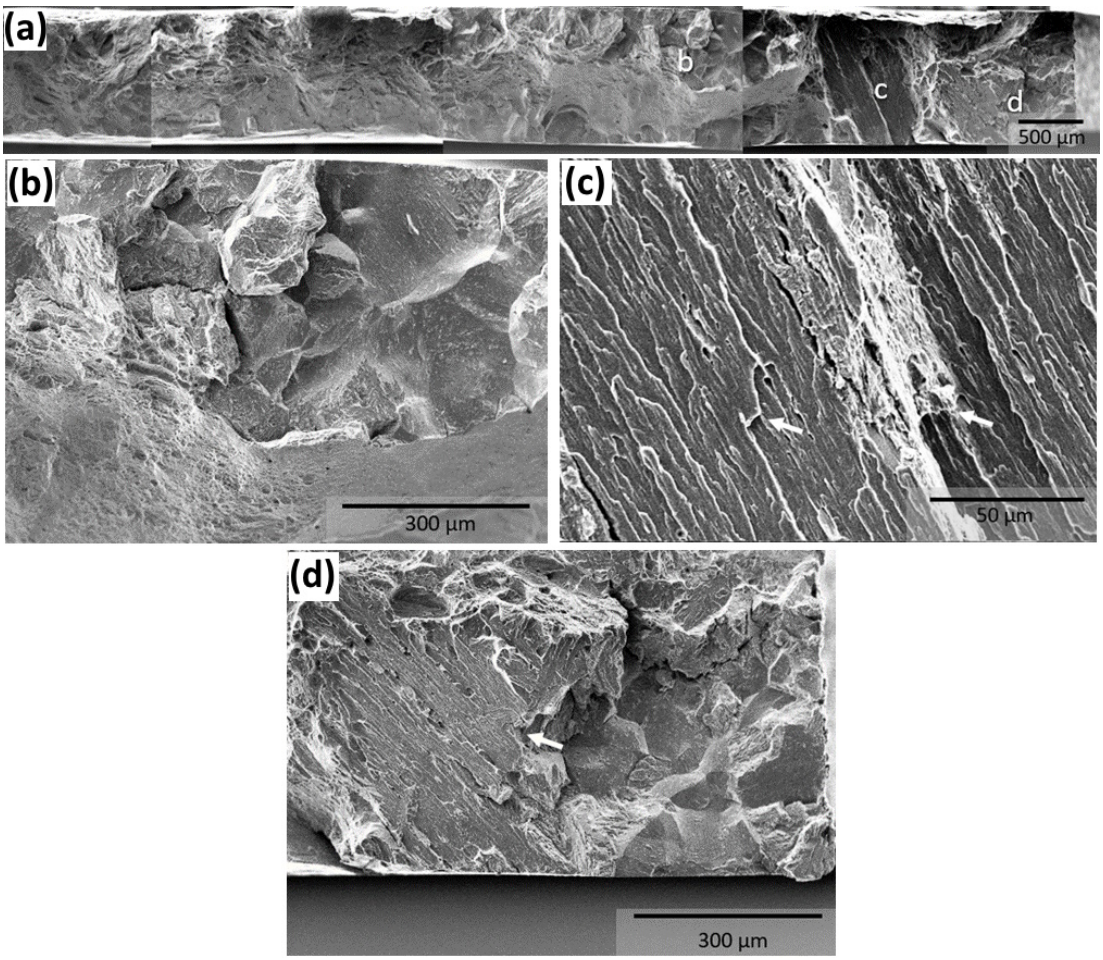


Figure 8. Fracture surface of Specimen D: (**a**)—general view; (**b**,**d**)—intergranular fracture zones whit cracks near the outer surfaces of the specimen; (**c**,**d**)—zones with clearly visible ridges, oriented in different directions.

3.5. TEM Analysis

The TEM images presented below were obtained from specimens subjected to relaxation tests. The specimen designations correspond to the hydrogen concentrations in the tensile-tested samples. These specimens did not exhibit a fracture zone; hence, the images were captured from the plastically deformed regions. The microstructural observations revealed two primary features: dislocations and slip bands.

A lath martensitic structure was observed in the steel samples investigated after heat treatment (Figure 9a). The lath widths varied unevenly, ranging from 50 to 650 nm. No distinct dislocation configurations were observed within the laths (Figure 9b).

In the specimens subjected to relaxation tests in air (Specimen A) (Figure 10), the dislocation structure did not significantly differ from that of the initial material. The dislocations were not of high density and were relatively evenly distributed within the observed plane. Increasing the hydrogen content led to a change in the dislocation localization. At low or negligible hydrogen concentrations, dislocations were primarily located in planes inclined to the lath boundaries (Figures 10a and 11a). As hydrogen concentration increased, dislocations were not only localized in planes inclined to the lath boundaries but also accumulated along the interfacial boundaries of the laths (Figure 11b). From the diffraction pattern, the dislocation localization plane was identified as (112) (inset of Figure 11b). Another notable feature observed was the formation of slip bands inclined to the lath boundary (Figure 11c).

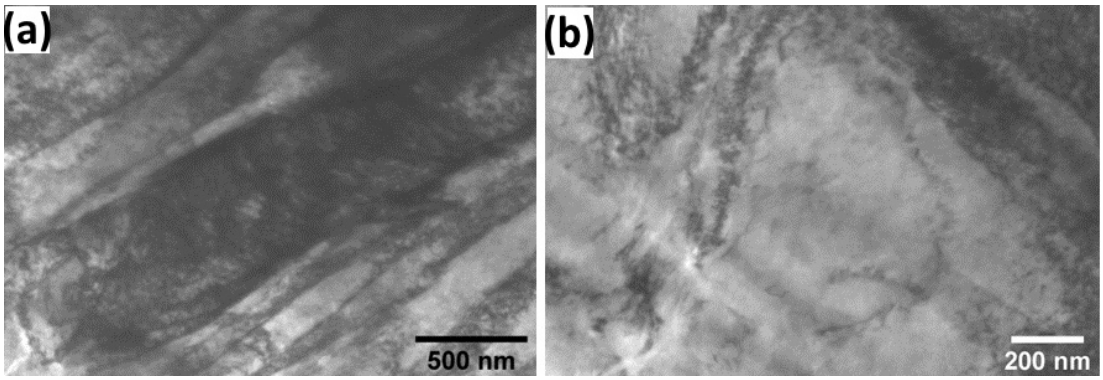


Figure 9. The microstructure of the investigated steel specimen after heat treatment. (**a**)—general view, (**b**)—magnified lath.

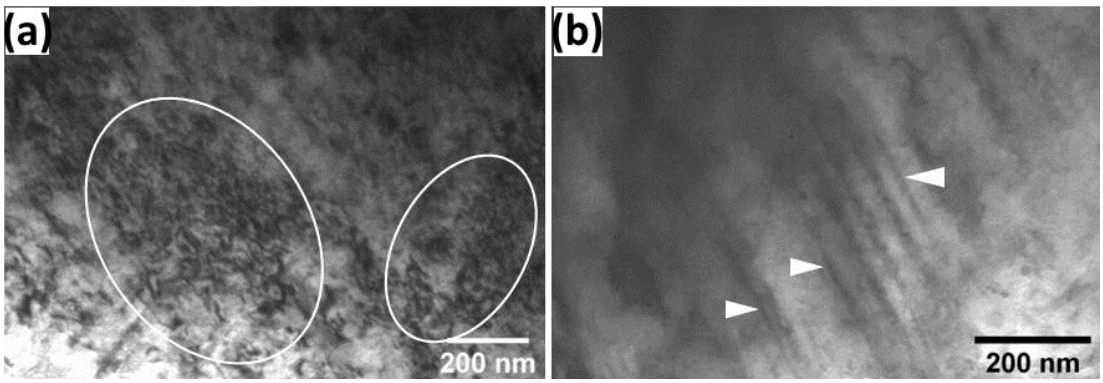


Figure 10. TEM images of Specimen A after relaxation tests: (**a**) the dislocation structure, with regions of higher dislocation density encircled; and (**b**) slip bands (marked with arrowheads).

Dislocation walls formed by dislocations localized along the lath boundaries were observed in specimens with higher hydrogen content (C and D) (Figures 12 and 13). In these samples, a higher concentration of slip bands inclined to the lath boundaries was observed, with longer lengths compared to the lower hydrogen content specimens. The underlying physics of the dislocation reorganization caused by hydrogen remains poorly understood. It is generally accepted that, for cell formation to occur, dislocations must be able to move out of their slip plane. Thus, the formation of cells depends on the factors that influence how easily dislocations can cross slip planes or climb. In [51], simulations and experiments were presented that demonstrated an increased likelihood of kink pair formation in secondary slip planes, as well as enhanced movement of dislocation segments out of the primary slip plane, in the presence of hydrogen. The formation of dislocation walls resulted in increased local stresses, which, in turn, heightened the likelihood of decohesion in the material. Increased dislocation activity and change in dislocation structure were observed at higher hydrogen concentrations. At the highest hydrogen concentration investigated, i.e., in Specimen D, the dislocations were observed to cross the lath boundaries (Figure 13c). In a study by Ohmura et al. [52], the interaction between dislocations and lath/block boundaries was investigated using nanoindentation tests. They found that dislocations tend to accumulate at block boundaries, and, under higher stresses, they cross the lath boundaries. This behavior suggests that the interfaces observed in our study are indeed lath boundaries.

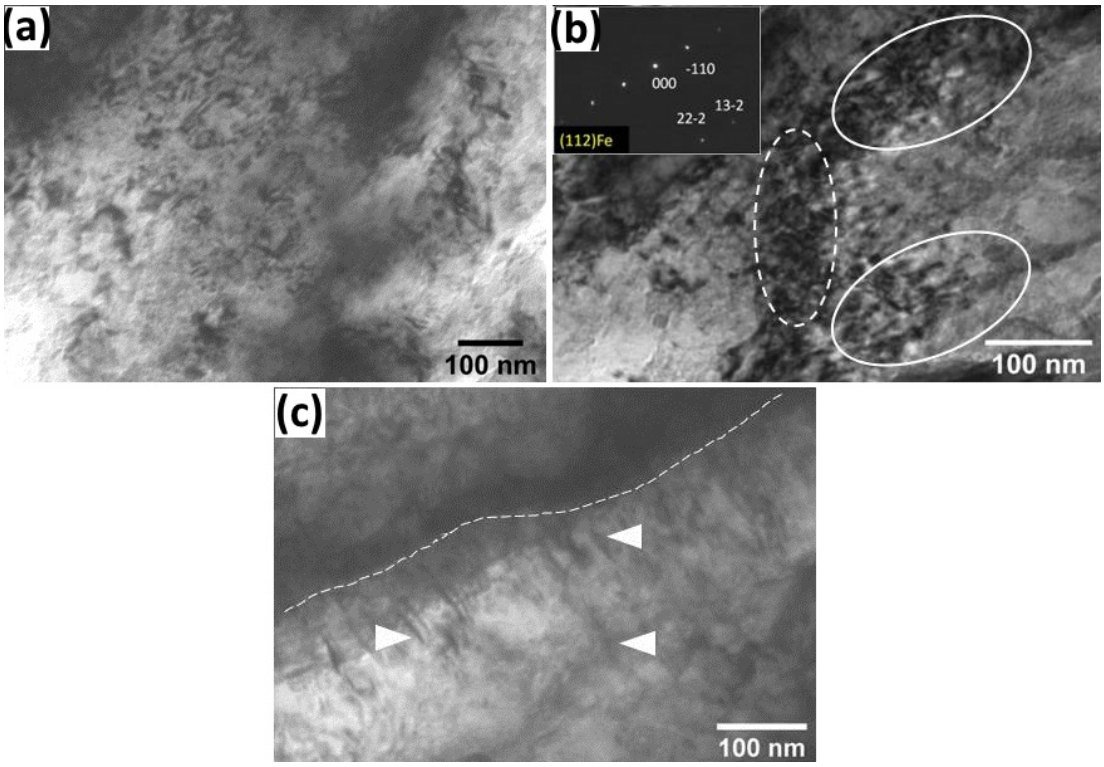


Figure 11. TEM observation of Specimen B: (**a**) dislocations with no specific configuration, predominantly located within the laths (the inset of (**a**) showed the SAED pattern corresponding to the observed (112) plane); (**b**) dislocations (encircled) were found along the lath boundaries and positioned in planes intersecting the interface (highlighted by a dashed line); and (**c**) slip bands (marked with arrowheads), with their development axis inclined to the lath boundary (marked by a dashed line).

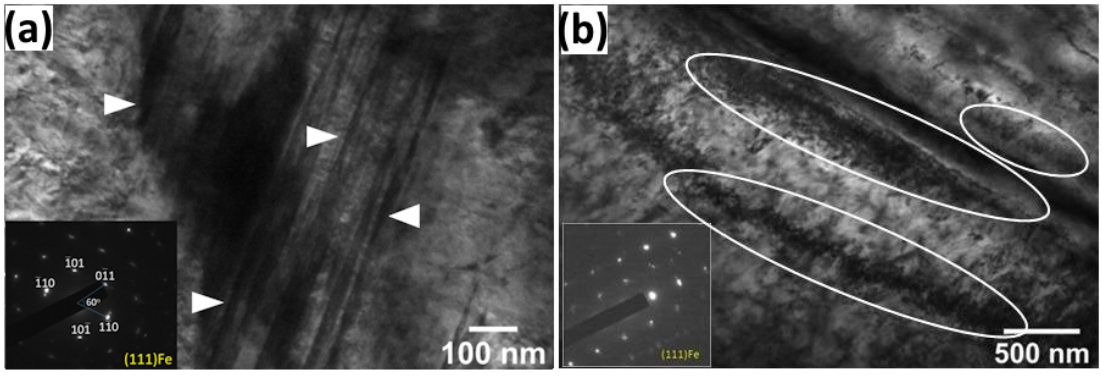


Figure 12. TEM observations of Specimen C: (**a**) slip bands (marked with arrowheads) (the inset in (**a**) shows the SAED pattern from the (111) plane); (**b**) dislocation localization along the lath boundaries, with the dislocation walls encircled (the inset displays the SAED pattern corresponding to the (111) plane).

As the hydrogen concentration increased, changes in dislocation density, localization, and the activation of slip systems were observed. The planes exhibiting the highest dislocation densities were the close-packed planes, specifically (111) and (100).

It was hypothesized that the slip bands intersecting the boundaries reduce the material's cohesive strength, and, when combined with hydrogen segregation at the lath/block boundaries, they promote the formation of quasi-cleavage fractures (via the HELP-mediated HEDE mechanism).

The exact mechanism of hydrogen-induced quasi-cleavage fracture in lath martensitic steels remains inconclusive [12,45,48,50,53–55]. Identifying the fracture planes associated with hydrogen-induced quasi-cleavage is crucial for determining whether the mechanism involves true cleavage. Two main groups of researchers have identified different planes—{110} and {100}—as the primary sites of quasi-cleavage fractures in these steels.

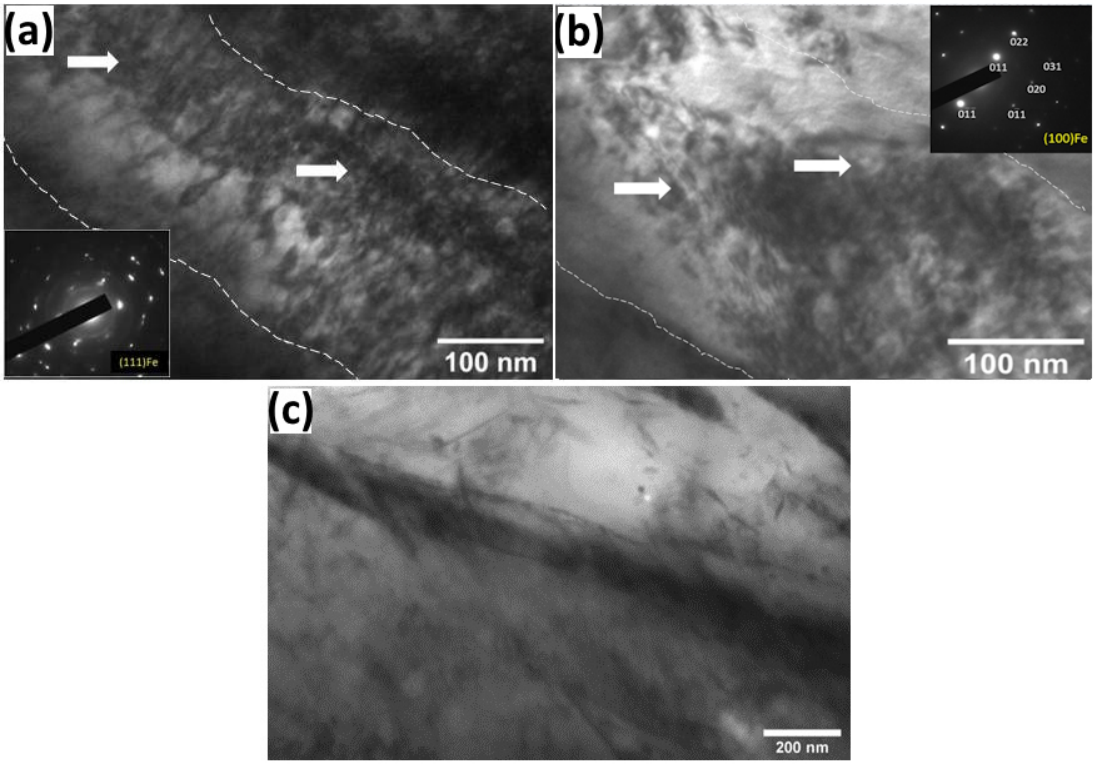


Figure 13. TEM observations of Specimen D: (**a**) dislocation localization along the lath boundaries (the inset shows the SAED pattern from the (111) plane); (**b**) an alternative dislocation configuration in planes inclined to the lath boundary (the inset of (**b**) displays the SAED pattern from the (100) plane); and (**c**) dislocations are observed to pass through the lath boundary. Dislocations are marked with arrows, and the boundaries are indicated by white dashed lines.

3.6. The Effect of Segregated H Atoms and Absorbed 1/2[111] Screw Dislocations on the Cohesive Strength of 10.53° Block Boundary—Atomistic Calculations

To better understand the mechanisms underlying the formation of "quasi-cleavage" cracks, we investigated the combined effect of the dominant mobile $1/2[111]$ screw dislocations in Fe, which were absorbed at a block boundary, and the hydrogen atoms segregated at that grain boundary on its cohesive strength. We considered a uniform separation of a bicrystal along a twist boundary parallel to the (110) plane in bcc Fe, which corresponded to a block boundary, under a tensile stress that was normally applied to the interface. To determine the cohesive strength of the interface, we calculated the excess surface energy density $e(\delta)$ versus the separation δ of the cohesive zone [56–58]. This excess energy $e(\delta)$ was obtained by atomistically calculating the energy of an elongated bicrystal composed of several atomic planes that were perpendicular to the direction of elongation. The excess energy was then derived from the following expression:

$$e(\sigma) = \frac{E(\sigma) - (n-1)E^e(\sigma)}{A}, \quad (4)$$

where $E(\sigma)$ is the energy of the separation along the twist boundary supercell at stress σ, $Ee(\sigma)$ is the elastic energy per plane of a homogeneously elongated crystal at the same stress σ, and A is the area of the supercell that is perpendicular to the direction of elongation [56,57]. The separation is given by

$$\delta(\sigma) = L(\sigma) - (n-1)l(\sigma) - d_0, \tag{5}$$

where $L(\sigma)$ is the length of the supercell at stress σ, $l(\sigma)$ is the length between the adjacent (110) planes in a homogeneously elongated crystal at the same stress σ, and d_0 is the equilibrium spacing between adjacent planes. The variable n is the number of atomic planes in the supercell that are perpendicular to the direction of elongation. In order to determine the cohesive strength of the block boundary, we fitted a universal binding curve [56,57,59],

$$e(\delta) = e_0 - 2\gamma(1 + \frac{\delta}{\lambda}) \exp{(\frac{-\delta}{\lambda})}, \tag{6}$$

to the atomistic calculations of the excess energy for different values of separation δ (Figure 14). The values of the unknown parameters $\gamma(\chi)$, $e_0(\chi)$ and $\lambda(\chi)$, in Equation (6) were determined as functions of the occupancy χ of the trap sites in the cohesive zone. Stress $\sigma(\delta)$ is the derivative of the energy $e(\delta)$ with respect to separation δ. The maximum of each traction curve $\sigma(\delta)$ was identified as the cohesive strength of the twist boundary. In the presence of hydrogen segregated at the GB, the excess variables and traction curve depended on the occupancy χ of the interfacial H trap sites.

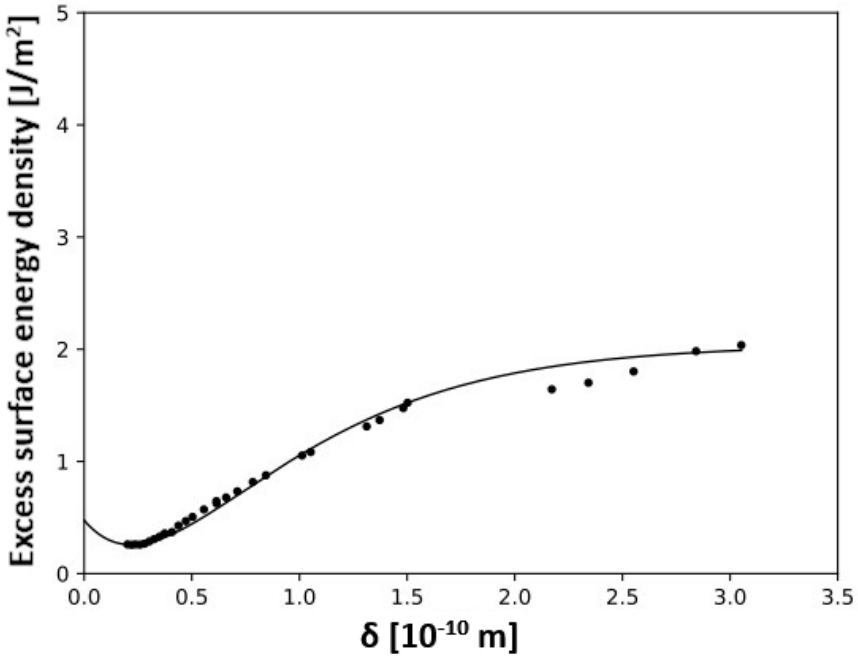


Figure 14. The excess surface energy density, which was calculated at different separations, was fitted to the universal binding curve. The H occupancy in the cohesive zone was 0.06.

In order to determine the excess variables, we constructed simulation boxes containing a block boundary with the lowest misorientation angle of 10.53°. The initial configuration of the bcc crystal was the $[21\bar{1}]$ direction as the X-axis, the [011] direction as the Y-axis, and the $[1\bar{1}\bar{1}]$ direction as the Z-axis in a Cartesian reference frame. The twist boundary was generated by rotating the upper and lower half of a perfect bcc crystal at the (011) midplane about the [011] direction. Two integers, k and m, generated a coincidence site lattice (CSL), which was designated by a parameter $\Sigma = 2k^2 + m^2$ for a twist angle $\varphi = 2arctan(\frac{m}{2\sqrt{2k}})$ [60], and Σ = 547 generated CSL for a 10.53° twist boundary, which ensured the application of periodic boundary conditions along the X- and Z-axes. The length of the periodic bicrystal in the X and Z directions was, correspondingly, 16.2 nm and 22.8 nm. The supercells contained n = 30 (011) planes that were perpendicular to the direction of elongation and consisted of 198,424 Fe atoms.

The results of the atomistic simulations revealed that the relaxed 10.53° twist boundary in bcc Fe was composed of hexagonal dislocation networks (HDN) (Figure 15a). The dislocation analysis shows that the networks of interfacial dislocations consisted of two families of intersecting near–screw dislocations with $1/2[111]$ Burgers vectors and screw [100] dislocations. The [100] screw dislocations were binary junctions of the intersecting $1/2[11\bar{1}]$ and $1/2[11\bar{1}]$ screw dislocations according to the reaction

$$\frac{1}{2}[1\bar{1}1] + \frac{1}{2}[11\bar{1}] \rightarrow [100], \tag{7}$$

where the $1/2[11\bar{1}]$ screw dislocations absorbed in the block boundary became part of HDN and modified its structure (Figure 15b). We calculated the excess energy for the fixed hydrogen occupancy χ and density of $1/2[11\bar{1}]$ screw dislocation absorbed in the GB by minimization of the total energy of the supercells for different separations. The lowest total energy was identified when the hydrogen atoms and screw dislocations were limited to the region of the twist boundary.

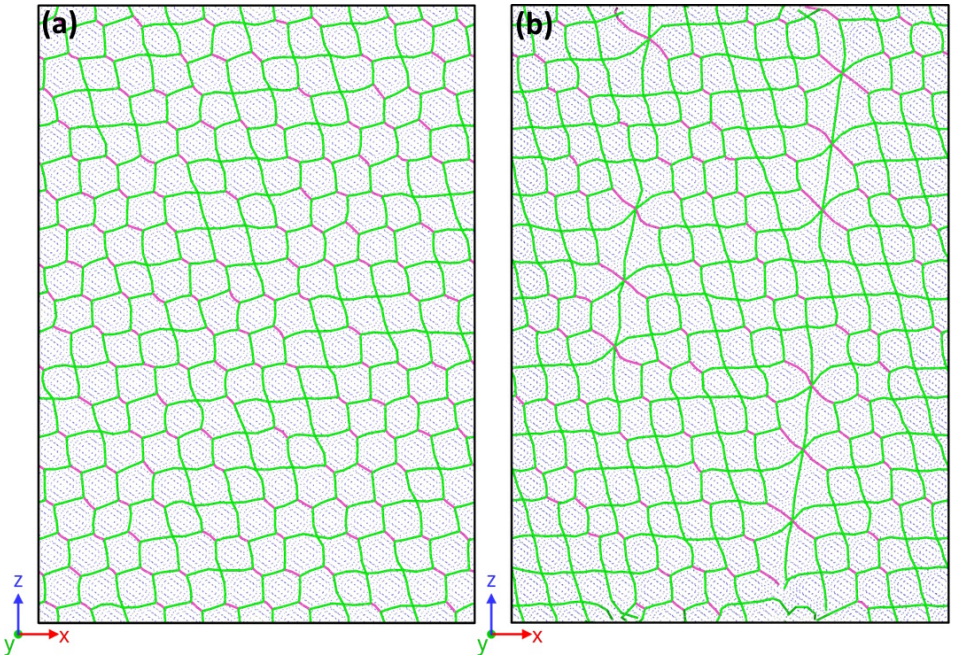


Figure 15. The structure of the 10.53° twist boundary in bcc Fe: (**a**) without absorbed dislocations, and (**b**) with absorbed $1/2[11\bar{1}]$ screw dislocations with a linear density of ρ_D = 0.25 nm^{-1}.

The corresponding family of traction curves calculated at five fixed values of the H occupancy in the cohesive zone is shown in Figure 16a.

The maximum of each traction curve was identified as the cohesive strength of the twist boundary at a fixed hydrogen occupancy in the cohesive zone. Our results show that the cohesive strengths of the twist boundary decreased almost twice in the presence of dissolved hydrogen occupying χ = 10% of the trap sites in the GBs. The $1/2[11\bar{1}]$ screw dislocations, absorbed at the block boundary with a linear density of ρ_D = 0.25 nm^{-1}, also reduced the cohesive strength of the interface, but the effect of the segregated H dominated (Figure 16b). However, hydrogen atoms can be transported by mobile dislocations. In order to be able to follow the dislocation, the H atoms trapped in the core need to diffuse at least as fast as the dislocation moves. Due to the strong attractive hydrogen binding region in the core of $1/2[111]$ screw dislocation and high mobility of H atoms in Fe, it is possible for screw dislocations to collect H atoms and to redistribute them [51,61,62]. According to the present atomistic simulations, we may assume that the hydrogen transported by dislocations absorbed at a block boundary affects the cohesive strength of the interface more than the effect caused by the modification of the GB structure. According to the present

atomistic simulations, we may assume that the hydrogen transported by dislocations absorbed at a block boundary affects the cohesive strength of the interface more than the effect caused by the modification of the GB structure.

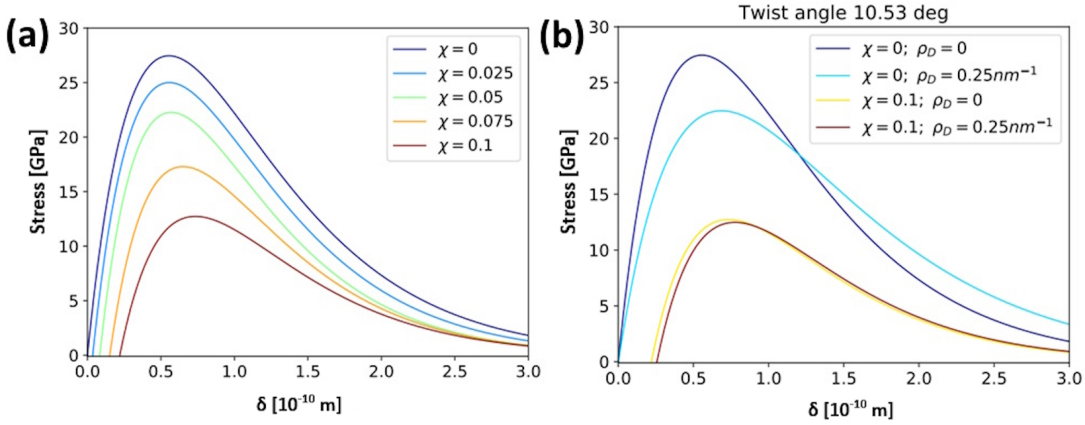


Figure 16. A family of traction curves corresponding to (**a**) the particular value of H occupancy, and (**b**) the particular value of H occupancy and the density of absorbed $1/2[11\bar{1}]$ screw dislocations.

The observed formation of the dislocation pile ups at the prior austenite and block boundaries that occurred by hindering the dislocation movement resulted in a greater local hydrogen accumulation at the interface due to the H transport by dislocations, which, consequently, reduced the cohesive strength of the boundaries. Dislocations absorbed in the block boundary modified the boundary structures and reduced its cohesive strength. In addition, increased dislocation density hardened the matrix and raised the local stress. The hydrogen accumulation on the "quasi-cleavage" fracture surfaces, where H was visualized using the hydrogen microprint technique [63], has been reported in [54].

Based on the results of the atomistic simulations and experimental observations, we conclude that 'quasi-cleavage' cracks predominantly initiate at block boundaries with higher local hydrogen accumulation. Both hydrogen and dislocations concentrated at the interface reduce the cohesive strength of the boundary, leading to crack openings when the cohesive strength falls below the local tensile stress. Crack propagation may slow when the crack tip encounters the regions of the block boundary with higher cohesive strength, which is due to lower hydrogen occupancy. However, as hydrogen accumulates at the block boundary through diffusion or transport by dislocation activity, the crack propagation along the interface is facilitated. This mechanism may explain why 'quasi-cleavage' fractures tend to propagate more gradually [64].

4. Conclusions

- Both experimental studies and atomistic modeling were conducted on hydrogen-charged, low-carbon lath martensitic steel.
- It was found that in hydrogen-charged, low-carbon martensitic steel, the fracture mechanism of the tensile-tested specimens changed with increases in hydrogen content. In the hydrogen-free specimen, the fracture was fully ductile. As the hydrogen concentration increased, the fracture mode transitioned from ductile to brittle. Initially, zones of transgranular quasi-cleavage fracture appeared, followed by the development of intergranular fracture zones.
- The critical hydrogen concentration for the studied specimens of the investigated steel did not exceed 0.44 wppm. At this concentration, a transition was observed from transgranular to intergranular fractures. The most likely cause of hydrogen embrittlement is the HELP-mediated HEDE mechanism.
- As the hydrogen concentration increased, dislocation density was observed to rise in the close-packed planes (111) and (100). The key differences between the hydrogen-free

and hydrogen-charged specimens were the localization and density of dislocations, as well as the increased density of the slip bands in the hydrogen-charged samples.
- Atomistic modeling showed that both the hydrogen and dislocations accumulated at the block boundaries reduce their cohesive strength. Crack initiation occurs when the local tensile stress exceeds the cohesive strength of the boundary. While the screw dislocations absorbed at the block boundary alter its structure and weaken the interface, the effect of segregated hydrogen—especially hydrogen atoms transported by dislocations at the boundary—dominates in reducing the cohesive strength.

Author Contributions: Conceptualization, I.K.; methodology, R.L., V.D. and B.Y.; software, I.K.; validation, I.K., V.D. and B.Y.; formal analysis, B.Y., Y.M., K.V., K.K. and J.K.; investigation, B.Y., V.D., Y.M., K.V., K.K. and J.K.; resources, V.D. and Y.M.; data curation, R.L.; writing—original draft preparation, V.D., Y.M., R.L. and K.V.; writing—review and editing, R.L., I.K., K.K., B.Y. and J.K.; visualization, I.K.; supervision, I.K. and R.L.; project administration, I.K. and R.L.; funding acquisition, I.K. All authors have read and agreed to the published version of the manuscript.

Funding: This research was financially supported by the Bulgarian National Science Fund (Project KP–06–N67/9 "Mechanism of Hydrogen Embrittlement in Lath Martensite Steel: Model Simulations and Experimental Study").

Data Availability Statement: The original contributions presented in the study are included in the article, further inquiries can be directed to the corresponding author.

Acknowledgments: The work in this publication was performed using equipment funded by project BG16RFPR002-1.014-0006 "National Center for Mechatronics and Clean Technologies".

Conflicts of Interest: The authors declare no conflicts of interest.

References

1. Ostash, O.; Vytvyts' kyi, V. Duality of the action of hydrogen on the mechanical behavior of steels and structural optimization of their hydrogen resistance. *Mater. Sci.* **2012**, *47*, 421–437. [CrossRef]
2. Lynch, S. Hydrogen embrittlement phenomena and mechanisms. *Corros. Rev.* **2012**, *30*, 105–123. [CrossRef]
3. Depover, T.; Van den Eeckhout, E.; Verbeken, K. The impact of hydrogen on the ductility loss of bainitic Fe–C alloys. *Mater. Sci. Technol.* **2016**, *32*, 1625–1631. [CrossRef]
4. Depover, T.; Escobar, D.P.; Wallaert, E.; Zermout, Z.; Verbeken, K. Effect of hydrogen charging on the mechanical properties of advanced high strength steels. *Int. J. Hydrogen Energy* **2014**, *39*, 4647–4656. [CrossRef]
5. Depover, T.; Laureys, A.; Pérez Escobar, D.; Van den Eeckhout, E.; Wallaert, E.; Verbeken, K. Understanding the interaction between a steel microstructure and hydrogen. *Materials* **2018**, *11*, 698. [CrossRef] [PubMed]
6. Birnbaum, H.K.; Sofronis, P. Hydrogen-enhanced localized plasticity—A mechanism for hydrogen-related fracture. *Mater. Sci. Eng. A* **1994**, *176*, 191–202. [CrossRef]
7. Robertson, I. The effect of hydrogen on dislocation dynamics. *Eng. Fract. Mech.* **1999**, *64*, 649–673. [CrossRef]
8. Ferreira, P.; Robertson, I.; Birnbaum, H. Hydrogen effects on the interaction between dislocations. *Acta Mater.* **1998**, *46*, 1749–1757. [CrossRef]
9. San Marchi, C.; Nibur, K.; Balch, D.; Somerday, B.; Tang, X.; Schiroky, G.; Michler, T. Effects of Hydrogen on Materials. In Proceedings of the 2008 International Hydrogen Conference, Jackson, WY, USA, 7–10 September 2008; pp. 88–96.
10. Troiano, A.R. The role of hydrogen and other interstitials in the mechanical behavior of metals. *Trans. ASM* **1960**, *52*, 54–81. [CrossRef]
11. Oriani, R.; Josephic, P. Equilibrium aspects of hydrogen-induced cracking of steels. *Acta Metall.* **1974**, *22*, 1065–1074. [CrossRef]
12. Nagao, A.; Smith, C.D.; Dadfarnia, M.; Sofronis, P.; Robertson, I.M. The role of hydrogen in hydrogen embrittlement fracture of lath martensitic steel. *Acta Mater.* **2012**, *60*, 5182–5189. [CrossRef]
13. Alp, T.; Dames, T.; Dogan, B. The effect of microstructure in the hydrogen embrittlement of a gas pipeline steel. *J. Mater. Sci.* **1987**, *22*, 2105–2112. [CrossRef]
14. Morito, S.; Tanaka, H.; Konishi, R.; Furuhara, T.; Maki, T. The morphology and crystallography of lath martensite in Fe-C alloys. *Acta Mater.* **2003**, *51*, 1789–1799. [CrossRef]
15. Kitahara, H.; Ueji, R.; Tsuji, N.; Minamino, Y. Crystallographic features of lath martensite in low-carbon steel. *Acta Mater.* **2006**, *54*, 1279–1288. [CrossRef]
16. Choo, W.; Lee, J.Y. Thermal analysis of trapped hydrogen in pure iron. *Metall. Trans. A* **1982**, *13*, 135–140. [CrossRef]
17. Wei, F.G.; Tsuzaki, K. Response of hydrogen trapping capability to microstructural change in tempered Fe–0.2 C martensite. *Scr. Mater.* **2005**, *52*, 467–472. [CrossRef]

18. Latypova, R.; Seppälä, O.; Nyo, T.T.; Kauppi, T.; Mehtonen, S.; Hänninen, H.; Kömi, J.; Pallaspuro, S. Influence of prior austenite grain structure on hydrogen-induced fracture in as-quenched martensitic steels. *Eng. Fract. Mech.* **2023**, *281*, 109090. [CrossRef]
19. Nagumo, M. *Fundamentals of Hydrogen Embrittlement*; Springer: Singapore, 2016.
20. Djukic, M.B.; Bakic, G.M.; Zeravcic, V.S.; Sedmak, A.; Rajicic, B. The synergistic action and interplay of hydrogen embrittlement mechanisms in steels and iron: Localized plasticity and decohesion. *Eng. Fract. Mech.* **2019**, *216*, 106528. [CrossRef]
21. Dmytrakh, I.; Syrotyuk, A.; Leshchak, R. Specific features of the deformation and fracture of low-alloy steels in hydrogen-containing media: Influence of hydrogen concentration in the metal. *Mater. Sci.* **2018**, *54*, 295–308. [CrossRef]
22. Dmytrakh, I.; Leshchak, R.; Syrotyuk, A.; Lutytskyi, O. Influence of the bulk concentration of hydrogen in the metal on the specific features of deformation of low-alloy pipe steel. *Mater. Sci.* **2014**, *50*, 170–178. [CrossRef]
23. *EN 10162:2003*; Cold Rolled Steel Sections—Technical Delivery Conditions—Dimensional and Cross-Sectional Tolerances. Bulgarian Institute for Standardization: Sofia, Bulgaria, 2003.
24. Garrison, W., Jr.; Moody, N. Hydrogen embrittlement of high strength steels. In *Gaseous Hydrogen Embrittlement of Materials in Energy Technologies*; Woodhead Publishing: Sawston, UK, 2012; pp. 421–492.
25. Chan, S.L.I. Hydrogen trapping ability of steels with different microstructures. *J. Chin. Inst. Eng.* **1999**, *22*, 43–53. [CrossRef]
26. Venezuela, J.; Zhou, Q.; Liu, Q.; Li, H.; Zhang, M.; Dargusch, M.S.; Atrens, A. The influence of microstructure on the hydrogen embrittlement susceptibility of martensitic advanced high strength steels. *Mater. Today Commun.* **2018**, *17*, 1–14. [CrossRef]
27. Capelle, J.; Dmytrakh, I.; Pluvinage, G. Comparative assessment of electrochemical hydrogen absorption by pipeline steels with different strength. *Corros. Sci.* **2010**, *52*, 1554–1559. [CrossRef]
28. Rahman, K.M.; Mohtadi-Bonab, M.; Ouellet, R.; Szpunar, J.; Zhu, N. Effect of electrochemical hydrogen charging on an API X70 pipeline steel with focus on characterization of inclusions. *Int. J. Press. Vessel. Pip.* **2019**, *173*, 147–155. [CrossRef]
29. Williamson, G.; Smallman, R., III. Dislocation densities in some annealed and cold-worked metals from measurements on the X-ray debye-scherrer spectrum. *Philos. Mag.* **1956**, *1*, 34–46. [CrossRef]
30. Saastamoinen, A.; Kaijalainen, A.; Porter, D.; Suikkanen, P.; Yang, J.R.; Tsai, Y.T. The effect of finish rolling temperature and tempering on the microstructure, mechanical properties and dislocation density of direct-quenched steel. *Mater. Charact.* **2018**, *139*, 1–10. [CrossRef]
31. Murugesan, S.; Kuppusami, P.; Mohandas, E.; Vijayalakshmi, M. X-ray diffraction Rietveld analysis of cold worked austenitic stainless steel. *Mater. Lett.* **2012**, *67*, 173–176. [CrossRef]
32. Macchi, J.; Gaudez, S.; Géandier, G.; Teixeira, J.; Denis, S.; Bonnet, F.; Allain, S.Y. Dislocation densities in a low-carbon steel during martensite transformation determined by in situ high energy X-Ray diffraction. *Mater. Sci. Eng. A* **2021**, *800*, 140249. [CrossRef]
33. *ISO 6892-1:2020*; Metallic Materials—Tensile Testing—Part 1: Method of Test at Room Temperature. Bulgarian Institute for Standardization: Sofia, Bulgaria, 2020.
34. Moshtaghi, M.; Safyari, M. Different augmentations of absorbed hydrogen under elastic straining in high-pressure gaseous hydrogen environment by as-quenched and as-tempered martensitic steels: Combined experimental and simulation study. *Int. J. Hydrogen Energy* **2023**, *48*, 27408–27415. [CrossRef]
35. Yanachkov, B.; Lyutov, L.; Katzarov, I.; Drenchev, L.; Kolev, K. Effect of Microstructure on the Mechanical Response of Hydrogen-Charged Pure Iron. *Metals* **2022**, *12*, 2160. [CrossRef]
36. Escobar, D.P.; Depover, T.; Wallaert, E.; Duprez, L.; Verhaege, M.; Verbeken, K. Thermal desorption spectroscopy study of the interaction between hydrogen and different microstructural constituents in lab cast Fe–C alloys. *Corros. Sci.* **2012**, *65*, 199–208. [CrossRef]
37. Morito, S.; Yoshida, H.; Maki, T.; Huang, X. Effect of block size on the strength of lath martensite in low carbon steels. *Mater. Sci. Eng. A* **2006**, *438*, 237–240. [CrossRef]
38. Nanayakkara, H. Phase-Field Modelling of Martensite Tempering in Steel. Master's Thesis, Interdisciplinary Centre for Advanced Materials Simulation, Bochum, Germany, 2021.
39. Vander Voort, G.F. Revealing prior-austenite grain boundaries. *Microsc. Microanal.* **2010**, *16*, 774–775. [CrossRef]
40. Lobodyuk, V.; Meshkov, Y.Y. Tetragonality and Real Crystal Structure of Martensite in the Carbon Steels. *Metallofizika i Novejsie Tehnologii* **2022**, *44*, 1575–1594. [CrossRef]
41. Masumura, T.; Inami, K.; Matsuda, K.; Tsuchiyama, T.; Nanba, S.; Kitahara, A. Quantitative evaluation of dislocation density in as-quenched martensite with tetragonality by X-ray line profile analysis in a medium-carbon steel. *Acta Mater.* **2022**, *234*, 118052. [CrossRef]
42. Degen, T.; Sadki, M.; Bron, E.; König, U.; Nénert, G. The highscore suite. *Powder Diffr.* **2014**, *29*, S13–S18. [CrossRef]
43. Martin, M.L.; Dadfarnia, M.; Nagao, A.; Wang, S.; Sofronis, P. Enumeration of the hydrogen-enhanced localized plasticity mechanism for hydrogen embrittlement in structural materials. *Acta Mater.* **2019**, *165*, 734–750. [CrossRef]
44. Bestautte, J.; Kalácska, S.; Béchet, D.; Obadia, Z.; Christien, F. Investigation of quasi-cleavage in a hydrogen charged maraging stainless steel. *Corros. Sci.* **2023**, *218*, 111163. [CrossRef]
45. Shibata, A.; Murata, T.; Takahashi, H.; Matsuoka, T.; Tsuji, N. Characterization of hydrogen-related fracture behavior in as-quenched low-carbon martensitic steel and tempered medium-carbon martensitic steel. *Metall. Mater. Trans. A* **2015**, *46*, 5685–5696. [CrossRef]

46. Guedes, D.; Malheiros, L.C.; Oudriss, A.; Cohendoz, S.; Bouhattate, J.; Creus, J.; Thébault, F.; Piette, M.; Feaugas, X. The role of plasticity and hydrogen flux in the fracture of a tempered martensitic steel: A new design of mechanical test until fracture to separate the influence of mobile from deeply trapped hydrogen. *Acta Mater.* **2020**, *186*, 133–148. [CrossRef]
47. Cho, L.; Bradley, P.E.; Lauria, D.S.; Martin, M.L.; Connolly, M.J.; Benzing, J.; Seo, E.J.; Findley, K.O.; Speer, J.G.; Slifka, A.J. Characteristics and mechanisms of hydrogen-induced quasi-cleavage fracture of lath martensitic steel. *Acta Mater.* **2021**, *206*, 116635. [CrossRef]
48. Beachem, C. Orientation of cleavage facets in tempered martensite (quasi-cleavage) by single surface trace analysis. *Metall. Trans.* **1973**, *4*, 1999–2000. [CrossRef]
49. Dieter, G.E. *Mechanical Metallurgy, 1988, Si Metric Edition*; Grawhill Book Company: London, UK, 2005.
50. Kim, Y.; Morris, J. The nature of quasicleavage fracture in tempered 5.5 Ni steel after hydrogen charging. *Metall. Trans. A* **1983**, *14*, 1883–1888. [CrossRef]
51. Gong, P.; Katzarov, I.H.; Nutter, J.; Paxton, A.T.; Rainforth, W.M. The influence of hydrogen on plasticity in pure iron—theory and experiment. *Sci. Rep.* **2020**, *10*, 10209. [CrossRef] [PubMed]
52. Ohmura, T.; Minor, A.; Stach, d.; Morris, J. Dislocation-grain boundary interactions in martensitic steel observed through in situ nanoindentation in a transmission electron microscope. *J. Mater. Res.* **2004**, *19*, 3626–3632. [CrossRef]
53. Ming, G.; Wei, R. Quasi-cleavage and martensite habit plane. *Acta Metall.* **1984**, *32*, 2115–2124. [CrossRef]
54. Nagao, A.; Smith, C.D.; Dadfarnia, M.; Sofronis, P.; Robertson, I.M. Interpretation of hydrogen-induced fracture surface morphologies for lath martensitic steel. *Procedia Mater. Sci.* **2014**, *3*, 1700–1705. [CrossRef]
55. Shibata, A.; Momotani, Y.; Murata, T.; Matsuoka, T.; Tsuboi, M.; Tsuji, N. Microstructural and crystallographic features of hydrogen-related fracture in lath martensitic steels. *Mater. Sci. Technol.* **2017**, *33*, 1524–1532. [CrossRef]
56. Van der Ven, A.; Ceder, G. The thermodynamics of decohesion. *Acta Mater.* **2004**, *52*, 1223–1235. [CrossRef]
57. Katzarov, I.H.; Paxton, A.T. Hydrogen embrittlement II. Analysis of hydrogen-enhanced decohesion across (111) planes in α-Fe. *Phys. Rev. Mater.* **2017**, *1*, 033603. [CrossRef]
58. Hirth, J.P.; Rice, J.R. On the thermodynamics of adsorption at interfaces as it influences decohesion. *Metall. Trans. A* **1980**, *11*, 1501–1511. [CrossRef]
59. Rose, J.H.; Ferrante, J.; Smith, J.R. Universal binding energy curves for metals and bimetallic interfaces. *Phys. Rev. Lett.* **1981**, *47*, 675. [CrossRef]
60. Warrington, D. The coincidence site lattice (CSL) and grain boundary (DSC) dislocations for the hexagonal lattice. *J. Phys. Colloq.* **1975**, *36*, C4-87–C4-95. [CrossRef]
61. Cottrell, A.H.; Bilby, B.A. Dislocation theory of yielding and strain ageing of iron. *Proc. Phys. Soc. Sect. A* **1949**, *62*, 49. [CrossRef]
62. Dadfarnia, M.; Martin, M.L.; Nagao, A.; Sofronis, P.; Robertson, I.M. Modeling hydrogen transport by dislocations. *J. Mech. Phys. Solids* **2015**, *78*, 511–525. [CrossRef]
63. Nagao, A.; Kuramoto, S.; Ichitani, K.; Kanno, M. Visualization of hydrogen transport in high strength steels affected by stress fields and hydrogen trapping. *Scr. Mater.* **2001**, *45*, 1227–1232. [CrossRef]
64. Shibata, A.; Matsuoka, T.; Ueno, A.; Tsuji, N. Fracture surface topography analysis of the hydrogen-related fracture propagation process in martensitic steel. *Int. J. Fract.* **2017**, *205*, 73–82. [CrossRef]

Disclaimer/Publisher's Note: The statements, opinions and data contained in all publications are solely those of the individual author(s) and contributor(s) and not of MDPI and/or the editor(s). MDPI and/or the editor(s) disclaim responsibility for any injury to people or property resulting from any ideas, methods, instructions or products referred to in the content.